

FINAL PUBLISHABLE REPORT

Grant Agreement number 16NRM07
 Project short name Vector SAR
 Project full title SAR measurement using vector probes

Project start date and duration:		01 May 2017, 36 months
Coordinator: Djamel Allal, LNE		Tel: +33 1 30 69 21 50
Project website address: http://empir.npl.co.uk/vectorsar/		E-mail: djamel.allal@lne.fr
Internal Funded Partners:	External Funded Partners:	Unfunded Partners:
1. LNE, France	4. ART-FI, France	
2. NPL, United Kingdom	5. IMTelecom, France	
3. TUBITAK, Turkey	6. KAPTEOS, France	
RMG: -		



TABLE OF CONTENTS

1. Overview 3

2. Need 3

3. Objectives 3

4. Results 4

 Objective 1: Develop traceable methods for the calibration of time-domain probes and probe arrays up to 6 GHz. In addition to verify the accuracy of such measurement systems after calibration and to determine the properties of associated sealed phantoms. 4

 Objective 2 Establish methods for uncertainty propagation through multivariate models, using the principles given in the ‘Guide to the expression of uncertainty in measurement’ (GUM). This will include identifying the sources of measurement uncertainties and their propagation through multivariate transformations for single vector probe systems and vector probe array systems. ... 9

 Objective 3 Verify the reliability of measurement systems for a wide range of transmitter types and improve the measurement of telecommunication signals and SAR measurement for a wide range of device types. This will include the development of improved data processing used with time-domain probes. 14

 Objective 4 Develop test protocols for MIMO devices using vector probe arrays in order to determine the maximum SAR value (worst case) by combining MIMO signal figures. 18

5. Impact 23

6. List of publications 24

7. Contact details 24

1. Overview

Specific absorption rate (SAR) is a measure of the rate at which energy is absorbed by the human body when exposed to a radio frequency electromagnetic field (EMF) and must be evaluated during the production of smartphones. The aim of this project was to provide the methods, software tools and datasets required for traceable calibration and uncertainty analysis of vector probe array systems (array of vector probes that automatically determines the 3D electromagnetic field mapping using amplitude and phase information through a 3D reconstruction algorithm), to measure the SAR of emitting mobile telecommunication devices. This work contributed to the international standard IEC 62209-3 and enabled the full-compliance of mobile telecommunication devices against IEC 62209-3 in terms of EMF exposure limits with better testing reliability, enabling testing times to be reduced, benefiting the telecommunications industry.

2. Need

Prior to the start of this project, the development of mobile phones was ever-increasing and approximately 1.3 billion smartphones were sold worldwide in 2014. In addition, the number of telecommunication protocols that need to be tested to assess SAR during the production of such smartphones has increased over the last decade. Therefore the methods included in the international standard IEC/IEEE 62209-1528 require excessively long testing times to assess compliance with SAR restrictions. For example, a modern smartphone with more than 30 transmission technologies/bands embedded would require five weeks of continuous testing to demonstrate compliance with SAR limits using the diode probe and robot specified in IEC/IEEE 62209-1528. In addition, not all foreseeable usage configurations are tested, e.g. the display of the phone is not facing towards the user and separation distances are shorter than that specified in the user manual. Furthermore, recent and upcoming communication standards, such as LTE Releases 10 and above, and 5G NR FR1, incorporate complex multiple-input multiple-output (MIMO) antennas that cannot be efficiently assessed using the systems specified in these standards, as these systems do not allow for electric field phase to be measured. Multi frequency measurement is also a challenge for traditional SAR measurement technologies as none of them have the capability to distinguish between frequency contributions to SAR. To overcome these problems, new SAR measurement systems have been developed which use arrays of vector probes, also called time-domain sensors, i.e. sensors which measure phase and amplitude to "image" the fields in a sealed phantom, a shell representing the human body, filled with a tissue-simulating liquid. Using this approach, the time required to acquire data for the SAR measurement of a handset is reduced by a factor of at least 100 compared to that using a traditional single probe scanning system. However, methods for traceable calibration and well quantified uncertainty estimates for these new systems were necessary, and were taken forward by this research before they can be adopted into documentary standards.

3. Objectives

The overall objective of this project was to provide the essential methods, software, data and validation required for the successful completion of the international standard IEC 62209-3 related to the measurement of SAR from handheld wireless telecommunications devices using vector based systems.

The specific objectives are to:

1. Develop traceable methods for the calibration of time-domain probes and probe arrays up to 6 GHz. In addition to verify the accuracy of such measurement systems after calibration and to determine the properties of associated sealed phantoms.
2. Establish methods for uncertainty propagation through multivariate models, using the principles given in the 'Guide to the expression of uncertainty in measurement' (GUM). This will include identifying the sources of measurement uncertainties and their propagation through multivariate transformations for single vector probe systems and vector probe array systems.
3. Verify the reliability of measurement systems for a wide range of transmitter types and improve the measurement of telecommunication signals and SAR measurement for a wide range of device types. This will include the development of improved data processing used with time-domain probes.
4. Develop test protocols for MIMO devices using vector probe arrays in order to determine the maximum SAR value (worst case) by combining MIMO signal figures.

- Facilitate the uptake of the developed measurement systems and contribute to the standards development work of the technical committee IEC - TC 106 on the successful adoption of IEC 62209-3 standard vector-based SAR measurement systems in Europe. In addition, to ensure that the outputs of the project are aligned with the needs of IEC - TC 106 and in a form that can be incorporated into the standards at the earliest opportunity.

4. Results

Objective 1: Develop traceable methods for the calibration of time-domain probes and probe arrays up to 6 GHz. In addition to verify the accuracy of such measurement systems after calibration and to determine the properties of associated sealed phantoms.

The technique developed for in-situ dielectric characterisation is presented first in this report. It uses two well-matched open-ended coaxial probes, Probe A and Probe B. The methodology developed can be applied when Probe A is freely-accessible, but Probe B is embedded permanently in the sealed tank by ART-FI after it has been initially characterised. The actual measurements were carried using different models of vector network analysers (VNA) and made in laboratory conditions in which measurements with both probes were made on samples in open beakers. The process of substitution calibration can be described as follows: Probe A is calibrated by the reference liquid method. The VNA test-port cable is then connected to Probe B, which is then used for measurements.

If the probes were identical then after the substitution no further action would be required in order to obtain traceable measurements. But, in order to account for differences between the probes, an additional step is needed where calibration of Probe B includes calibration data of Probe A.

The two open-ended coaxial probes, which are nominally identical, were manufactured at NPL according to the design shown in Figure 1. A photograph of one of the probes is also shown. They are based on 7 mm coaxial line and are similar to an earlier design, but longer and with fittings appropriate for a tank. The flange diameter is 25 mm. A VNA is connected to the probe via a metrology-grade phase-stable cable.

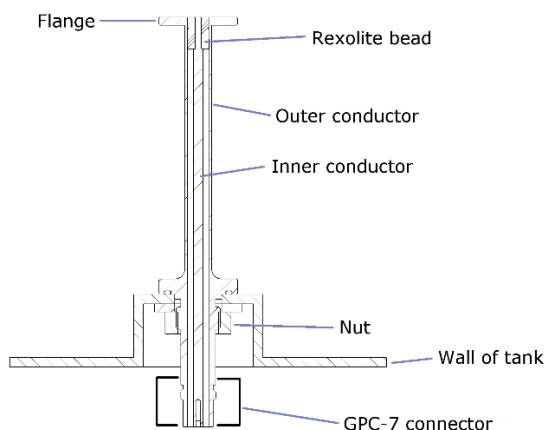


Figure 1. Design (left) and photograph (right) of the nominally identical 7 mm open-ended coaxial probes that are used for monitoring a liquid in a sealed tank. A calibration scheme that takes account of the inaccessibility of the flange is required.

The probes can be calibrated individually by using measurements on a short-circuit, an open-circuit and a reference liquid for which traceable complex permittivity data as a function of temperature are available. Two reference-liquids are used in combination for calibration: methanol in the band between 2.5 GHz and 6 GHz and ethanol for frequencies below 2.5 GHz, to obtain the best results with regards to their respective properties in terms of frequency.

Measurements on dimethyl sulphoxide taken as verification liquid were found to be in good agreement with the reference data. Measurements on a tween-based tissue-equivalent liquid made with Probe B by using the substitute calibration were found to agree well with the measurement made by using Probe A. It is expected that the uncertainty of measurements made with Probe B (for the substitution method of calibration using Probe A) will be increased by approximately $\sqrt{2}$ (as independent calibrations on two probes are used). This would appear to be consistent with this evaluation of uncertainty.

Some 9 months after the above tests were completed at NPL, the open-ended coaxial probes, a sample of the tween-based tissue-equivalent liquid, and a file of coefficients linking Probe B to Probe A were shipped to LNE for independent tests. Probe A was calibrated by the reference liquid method and used to measure the same sample of tween-based tissue-equivalent liquid. The tissue-equivalent liquid was then re-measured with Probe B after applying the substitution method of calibration. The results in Figure 2 show good agreement between the techniques, and show that the tween sample has not significantly changed its properties in 9 months. Deviations between the measurements are small compared to the 10% tolerance that is specified for tissue-equivalent liquids used for SAR measurement. The viability of the substitution method for calibration is thus demonstrated.

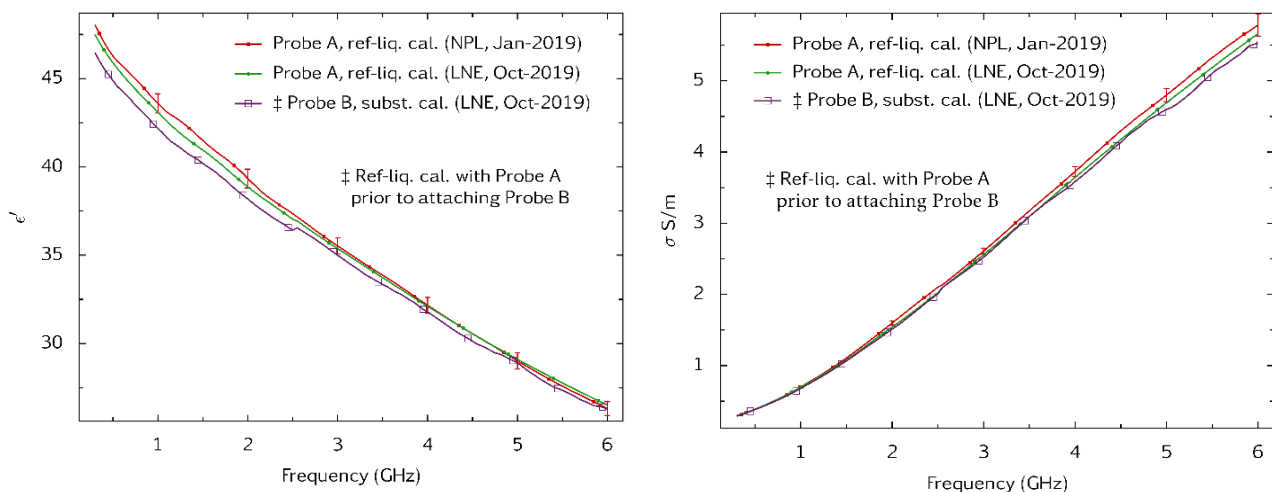


Figure 2. Measurements of the dielectric properties ϵ' (left) and σ (right) on the same sample of a tween-based tissue equivalent liquid. Measurements with Probe A were made at NPL and, after a 9-month interval, at LNE. Probe A was calibrated at both laboratories by the reference liquid method. LNE also measured the specimen with Probe B, using the substitution method.

Regarding the calibration procedure of vector probes for vector probe arrays traceability, and as planned, high accuracy reference antennas of the Vivaldi type, suitable for 900 MHz, 2450 MHz and 5200 MHz were designed and fabricated by ART-FI and provided to NPL for measuring vector E-field data obtained inside a reference phantom for these antennas. Photographs of these antennas are shown in Figure 3.

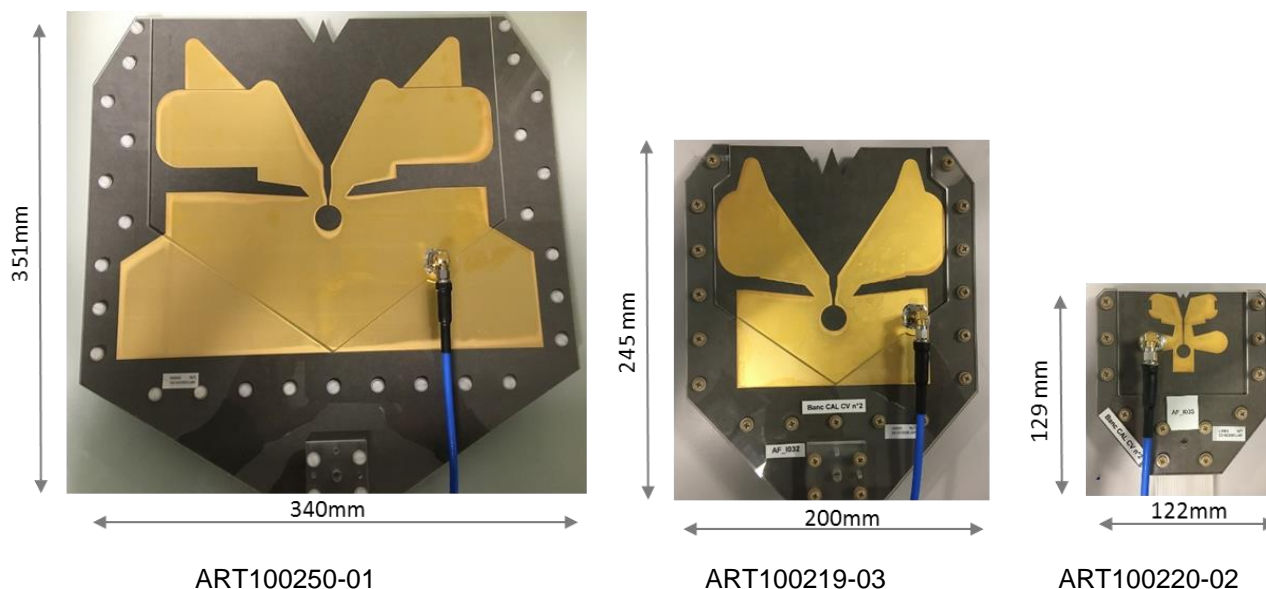


Figure 3. Photograph of the designed and fabricated reference antennas of the Vivaldi type and their dimensions, suitable for 900 MHz, 2450 MHz and 5200 MHz, respectively from left to right.

The calculable validation antennas for use also at 900 MHz, 2450 MHz and 5200 MHz were existing dipole antennas provided by NPL, compliant with the IEC 62209 standards. Their role is to validate SAR measurements produced by any array-based SAR measurement system.

The SAR induced in a phantom is obtained by modelling and by comparison to measurements obtained by using a scalar E-field probe. A calibration procedure has been devised with the aim to establish traceable maps of vector E-field (magnitude and relative phase) inside a phantom. Also, traceable maps of SAR inside a phantom illuminated by the validation antennas are carried out by using established methods of measuring SAR with scalar probes. This data are then used for developing and demonstrating a procedure for evaluating the precision of array-based systems (as per objective 3).

The procedure that was developed is described as follows. First the calibration of the magnitude response of a vector probe that can be used for mapping vector E-fields is carried out in a waveguide cell. The sensitivity of E-field probes depends on the dielectric permittivity of the surrounding medium, so they must be calibrated against calculable fields while immersed in a phantom liquid. The permittivity and conductivity of the liquid must comply with the specifications given in international standards for SAR measurement. Existing waveguide cell systems used for calibration of scalar E-field probes were modified to allow calibration of vector E-field probes. Second, the mapping of vector electric field is carried out over a defined X-Y plane by using a vector E-field probe that is calibrated for in-phantom measurements.

Two models of vector probes were available within the project. The model manufactured by KAPTEOS and a model from Seikoh-Giken available at NPL in charge of the task. Due to practical reasons, the latter was used, which allowed to allocate more time to setting up the experiment and doing several measurement campaigns. This probe is of the electro-optic type. It contains no metal other than a miniature dipole that is fabricated on a lithium niobate substrate. The signal, after amplification, is measured by a VNA. The electro-optic probe used in this work is very small (dipole antennas approximately 2 mm in length) to minimise disturbance to fields being measured. This has the consequence that the associated detection system (VNA) must have high sensitivity. The VNA was used at its lowest IF bandwidth setting (10 Hz), otherwise there would have been insufficient signal compared to the noise.

An advantage of using a vector probe is that the boundary condition $E_x + E_y + E_z = 0$ can be applied to obtain E_z if E_x and E_y are measured in the near field, i.e. three field components can be obtained from two measurements.

As the E-field present in the waveguide cell is calculable from traceable measurements, the E-field in the phantom can be measured traceably. True vector measurements are made, but the recorded phase is only relative as no reference plane is defined.

Traceability of E-field in the waveguide cell is well established. E-field magnitude is calculated from

$$E^2(z) = \frac{4P_{WG}}{ab\delta\sigma} \exp\left(-\frac{2z}{\delta}\right)$$

where P_{WG} is the power flowing in the waveguide at the interface between the liquid and the window, ab is the area of the waveguide, δ is the skin depth in the phantom liquid, σ is the conductivity of the phantom liquid and z is the distance from the sensing element inside the probe to the top of the dielectric window.

The calibration factor $F(z)$ of the vector probe is obtained from the waveguide cell measurements from the system equation $F(z) = E(z)/T(z)$, where $E(z)$ is the calculated field and $T(z)$, equivalent to $|S_{21}|$, is measured by the VNA. $F(z)$ is determined from measurements made with the sensing axis inside the probe aligned according to the direction of the E-field in the waveguide, that is, parallel to its narrow dimension.

Then the E-field pattern is measured in the reference phantom while it is illuminated by the reference antenna. Components associated with the signal path such as the VNA, couplers and cables are unchanged compared to the first experiment (in the waveguide cell), and the system equation therefore remains valid if the power level is unchanged and a substitution is carried out.

By using a robot scanning system, the E-field inside the reference phantom is mapped over a plane and in the two angles of rotation of the sensing axis of the probe. (0° and 90°), and the relative phase of measurements is also recorded as to make vector measurements.

Figure 4 shows a plot of the magnitude of the X-component of the electric field measured in the reference phantom illuminated from beneath, at a specified distance, by a reference antenna (ART100250-01). As vector measurements were performed, complex values of the X- and Y-components of the electric field were obtained at each scanned location.

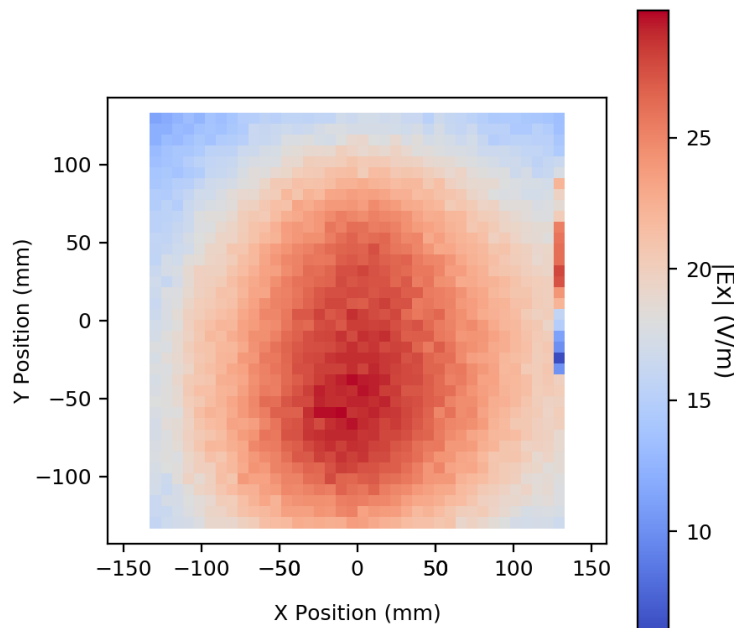


Figure 4: Colour map of the magnitude of the X-component ($|E_x|$) of the E-field in the reference phantom at height $z = 10$ mm. This data was obtained for reference antenna ART100250-01 at 900 MHz. The antenna was 10 mm beneath the phantom. They are determined for an input power of 1.66 W.

In summary, traceable methods have been set up for the calibration of time-domain probes and probe arrays up to 6 GHz, first, by developing a methodology to traceably characterise the electromagnetic properties of sealed phantoms and second, by developing the process for characterising a reference antenna through mapping of complex E-field in the phantom using an electro-optic time-domain probe traceable to a waveguide E-field standard and providing so traceability to the vector array used for measuring the E-field in the same phantom.

Objective 2 *Establish methods for uncertainty propagation through multivariate models, using the principles given in the ‘Guide to the expression of uncertainty in measurement’ (GUM). This will include identifying the sources of measurement uncertainties and their propagation through multivariate transformations for single vector probe systems and vector probe array systems.*

The vector fields measured in a phantom have real and imaginary parts $E_x = E'_x + jE''_x$ and $E_y = E'_y + jE''_y$. These fields are calculated using calibration factor F and vector transmission coefficient S_{21} . The uncertainties associated with the E-field components are evaluated from the uncertainty associated with F , and the uncertainty associated with S_{21} measured by the robot scan. S_{21} is resolved in both x and y directions, which are here referred to as $(S_{21})_x = T'_x + jT''_x$ and $(S_{21})_y = T'_y + jT''_y$. Uncertainties associated with the measured quantities from which F is calculated (calibration in the waveguide cell) must first be identified and then evaluated. Figure 5 shows the process used by NPL for evaluating uncertainty associated with measured E-fields in the reference phantom. The Type B contribution associated with the determination of F in the waveguide cell is shown above the dotted line. In order to account for the change in environment (from the waveguide cell to the reference phantom), an additional uncertainty contribution, shown beneath the dotted line, is applied. Finally, the Type A component is obtained based on the repeatability of E-field measurements made during scans with the robot.

The Type B uncertainty associated with F (using the waveguide cell) is determined from contributions due to input power, waveguide power transmission fraction and dimensions, liquid conductivity and temperature and transmission coefficient S_{21} . Scanned measurements on the reference phantom illuminated by the different reference antennas were performed three times to allow evaluation of the Type A uncertainty. Type A contribution at 900 MHz and 2450 MHz are evaluated as 1.4 V/m and 2.5 V/m, respectively. Note that for 5200 MHz signal to noise ratio was very poor, and better measurement system specifications will be needed to allow reliable uncertainty assessment. Following the scheme advocated in Figure 5, the uncertainty can be calculated as follows: For example, the calibration factor at 900 MHz was $F = 32938$ V/m per S-parameter unit and its standard uncertainty is evaluated as 2343 V/m per S-parameter unit. Therefore if $E = 30$ V/m then $T = 30/32938 = 0.0009$, and $u(|E_x|) = \sqrt{(1.4 \text{ V/m})^2 + (2343 \text{ V/m} \times 0.0009)^2} = 2.5 \text{ V/m}$.

The measurement uncertainty associated with $|E_x|$ is approximately 15% at coverage factor $k = 2$ in a high E-field region (30 V/m). The Type A contribution associated with the scanned measurements is larger than the Type B contribution associated with the calibration in the waveguide cell. This is partly because the E-fields in the reference phantom are weaker than those in the waveguide cell, so S_{21} is closer to the noise floor.

An assessment of relative phase uncertainty was also made on the basis of measurements in high E-field locations (to ensure that measurements of T significantly exceed the associated random noise). Only relative phase is measured; therefore the requirement is to evaluate the uncertainty caused by phase drift during each scan with the robot, rather than between one scan and another. A point at the same (high E) location for the three scans was chosen as a phase reference point. Point-to-point phase variations within each set relative to this point were then calculated. The Root Mean Square phase drift between three scans was used as the basis of the uncertainty evaluation. The expanded uncertainty associated with the relative phase obtained at 900MHz and 2450 MHz are respectively 1.4° and 4.3° at coverage factor $k = 2$.

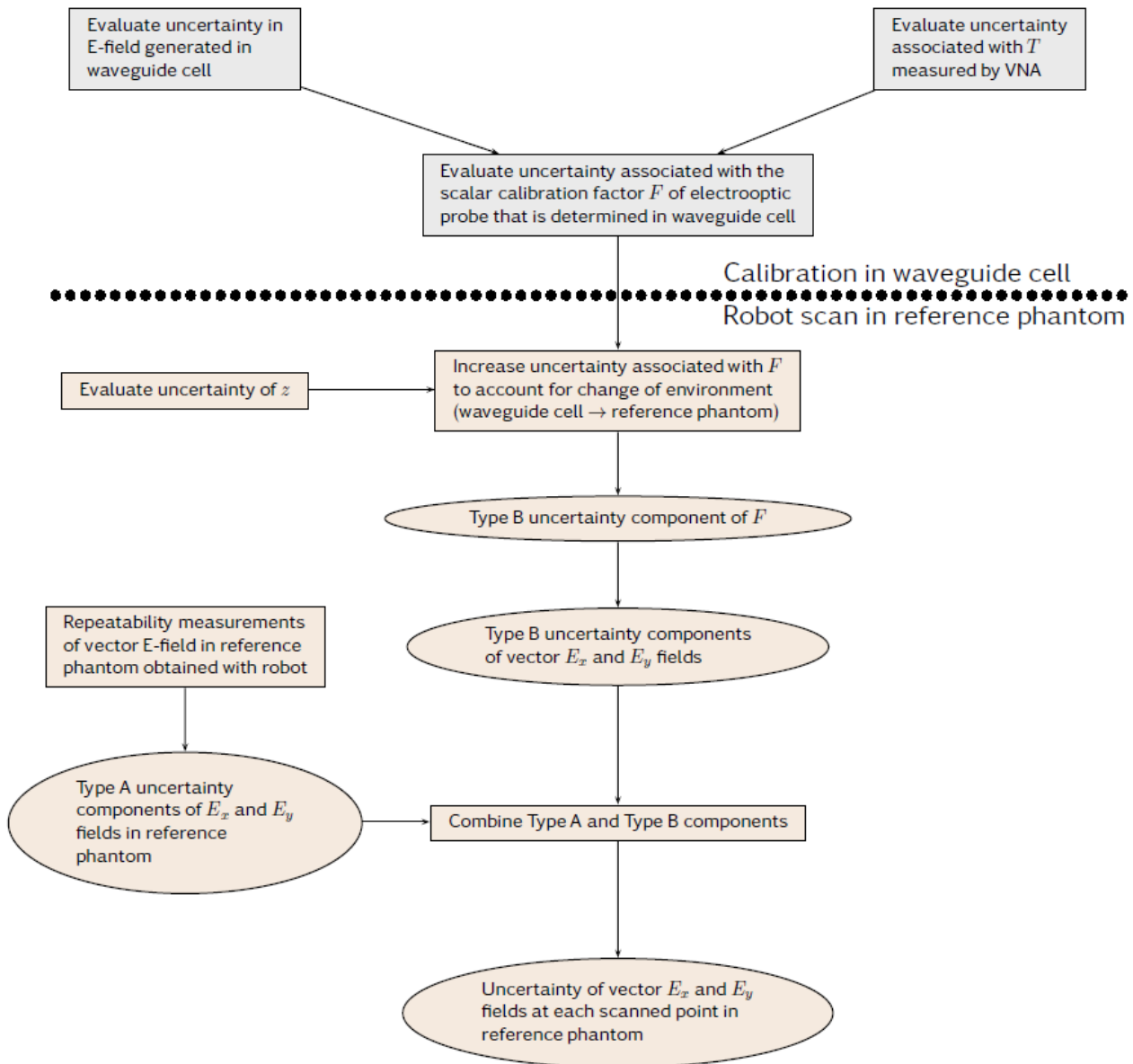


Figure 5: The process used to evaluate uncertainty

Uncertainty propagation models for determining the uncertainty in the 1 g or 10 g peak averaged SAR values when the calibrated vector probe array system is used to measure sources are provided below. These are based on a MATLAB code, developed by IMTelecom, which generates the matrix of uncertainty components for each sensor in a vector probe array. It is part of the development of methodologies using specific statistical methods for determining the uncertainty in the 1 g or 10 g peak averaged SAR values when the calibrated vector probe array system is used to measure the SAR of radiating sources.

The software carries out the uncertainty analysis of the estimation of 1 g and 10 g peak spatial-average SAR using complex uncertainty propagation models of the vector probe array transfer function together with reference field distributions to perturb the inputs. It allows the assessment of the effects on the measurand and the estimation of the sensitivity coefficients.

The uncertainties of probe position, accuracy of measured electric fields, coupling effects from neighbored probes, and electromagnetic properties of the phantom are considered and analysed with Monte Carlo simulations. The random samples of the uncertain factors are generated with Latin Hypercube sampling

method and each sample is dealt with independently. The uncertain electromagnetic properties are considered by putting deviations on permittivity and conductivity of the phantom. With the true wavenumber of the phantom, the reference analytical functions yield the electric fields measured by a vector probe array but at perturbed probe positions. The coupling effects from neighbour probes are quantified by coupling coefficients. The accuracy of measured electric fields is considered by assuming the error of amplitude and phase follows specific distributions.

With the measured electric fields, the fields in the interested region are reconstructed and the 1 g and 10 g SAR peak spatial-average SAR are estimated. The applied field-reconstruction algorithm is based on plane-wave expansions. The performance is related with the parameter δ , the value of which is related with the trade-off between estimation precision and estimation reliability.

The code generates values of 1 g and 10 g SAR peak spatial-average SAR for Monte Carlo simulations. Based on the estimations, the sensitivity of the concerned uncertain factors can be obtained by computing the Sobol indices.

The code simulates the estimation process of a vector probe array system based on field reconstruction and analyses the uncertainty by Monte Carlo simulations. The technique of plane wave expansion is applied for the field reconstruction.

The probes in the considered probe array measure the amplitude and phase of electric fields on a single plane. The solution to fields at other positions of interest is obtained by a field-reconstruction algorithm.

The planar wave expansion theory represents the electric field as an integral of planar waves, which gives

$$E(x, y, z) = \frac{1}{4\pi^2} \int_{-\infty}^{\infty} \int_{-\infty}^{\infty} \tilde{E}(k_x, k_y) e^{i(k_x x + k_y y - k_z z)} dk_x dk_y$$

Where (x, y, z) is the Cartesian coordinates of the observation point and k_x, k_y, k_z are respectively the x, y, z component of the wavenumber k of the liquid. The electric field is then seen as a two-dimensional inverse Fourier transform of $\tilde{E}(k_x, k_y) e^{-ik_z z}$ and can be reconstructed if the corresponding spatial-frequency spectrum is known.

Electric fields are measured on a plane with probes uniformly distributed in a specific domain, whose centre is usually within the main lobe of the radiated field and is used to define the probes coordinates in the x and y directions of the 2D measurement plane. Mathematical analysis allows to reconstruct the 3D field $E(x, y, z)$ as a 2D plane by plane reconstruction, starting from the initial 2D field $E(x, y)$ corresponding to the measurement plane.

The studied system has the source under test placed at 5 mm from the phantom and the vector probe array at the plane $z = 19.25$ mm. An array of 29×29 probes is uniformly distributed in the surface defined by $-10 \text{ cm} < x, y < 10 \text{ cm}$ with interval 7 mm. For analysis purposes, probes are represented as points and measurements of electric fields are assumed to be traceable to a single vector probe scan in the same phantom on the same plane. The measured electric field inside the phantom is obtained based on the analytical function.

The post-processing includes the field reconstruction of regions of interest and the followed computation of peak spatial-average SAR. The former is verified by observing the reconstructed field on the plane of $z = 0$ mm and comparing with the reference as shown in Figure 6 for frequency 2450 MHz, where the maps of field intensity in the first row are the reference, the second row gives the reconstructed results, and the last row shows the absolute error of reconstruction. The resolution of the map is 2 mm. For this case, the liquid parameters are 39.37 and 1.45 S/m for the relative permittivity and the conductivity, respectively, and the reference value of peak 10 g SAR is 0.431.

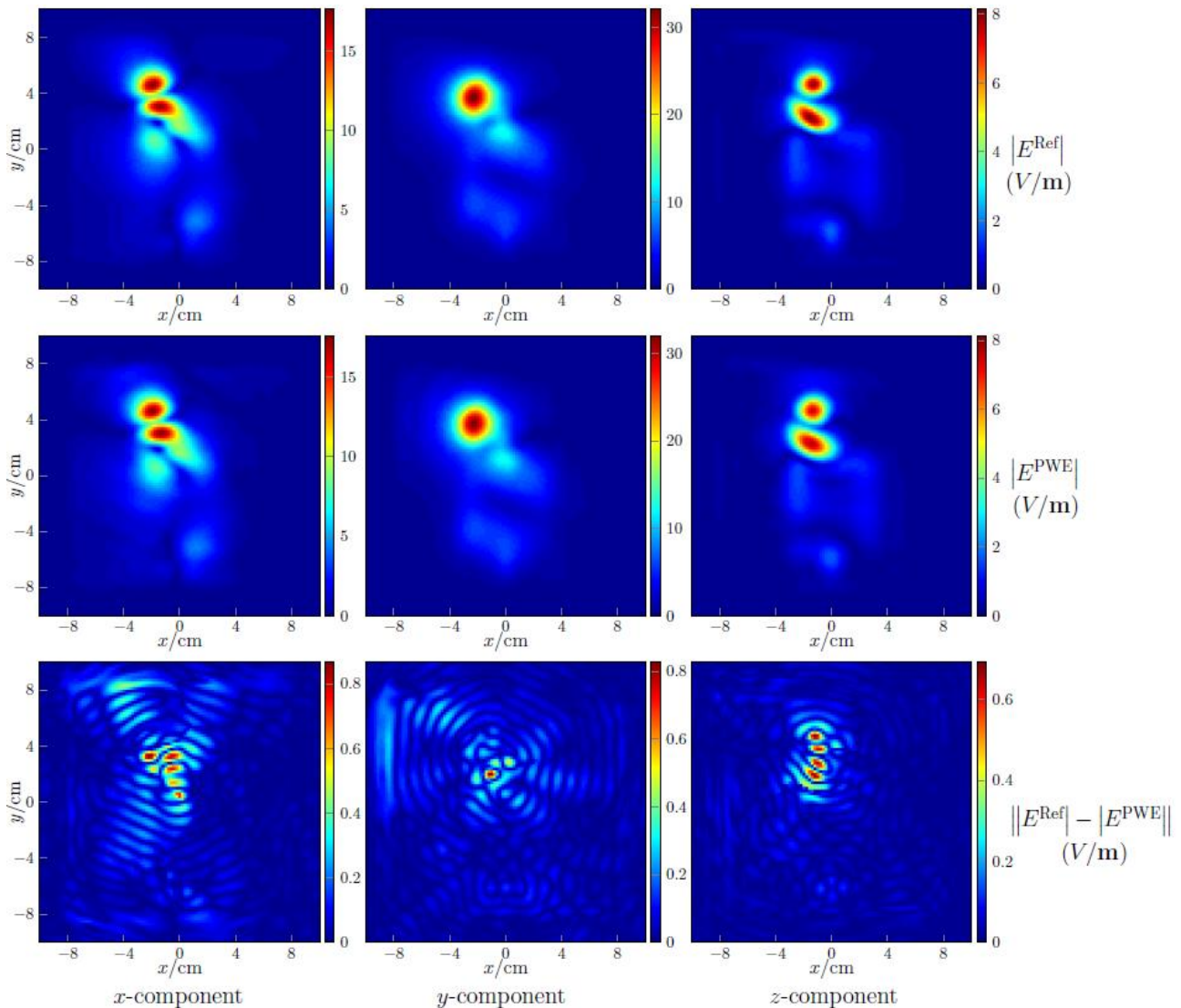


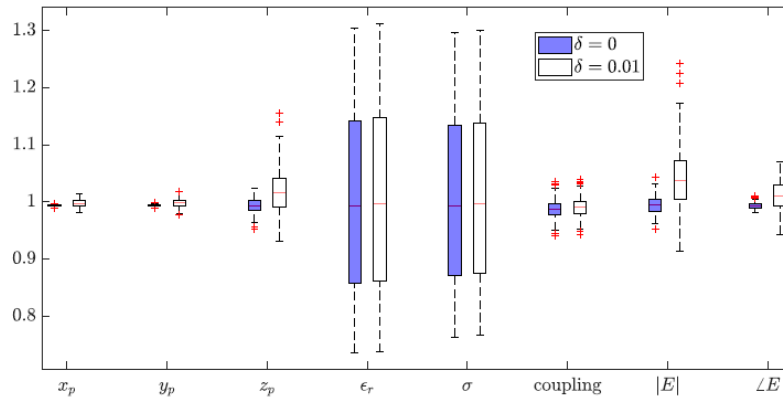
Figure 6: Field reconstruction with respect to the fourth case. E^{PWE} and E^{Ref} denote the reconstructed field and the reference (measured) field, respectively

As seen, the amplitude of the reconstructed fields is a little different from the reference, the absolute errors being small. Setting the resolution as 1mm, with the reconstructed field of the cube bounded by $-10 \text{ cm} < x, y < 10 \text{ cm}$, $0 \text{ cm} < z < 3 \text{ cm}$ the computed peak spatial-average SAR equals 0.993 for 1 g and 0.427 for 10 g, which are quite close to the reference values 1 and 0.431.

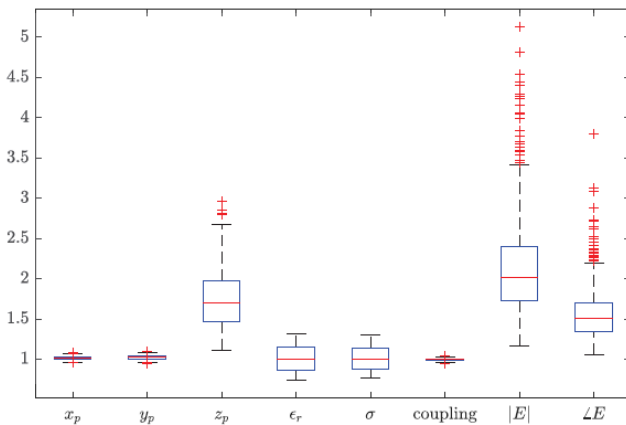
An uncertainty budget is established for which the principal contributions are the Cartesian coordinates of each probe position, the relative permittivity and the conductivity of the liquid, the amplitude and the phase angle of the electric field. Moreover, the mutual inductance among probes yields the so-called coupling effects (correlation coefficients). In practice, since the composition of probes may not be exactly the same, the coupling effects can differ for different pairs of probes and are hard to be analysed due to many involved coupling coefficients. Here, the coupling effects of each probe are analysed by only taking into account the mutual inductance from its eight neighbour probes.

Monte Carlo method of uncertainty estimation is applied and estimated peak 1 g SAR for the 2450 MHz case is shown in Figure 7 indicating the uncertainty of all contributing factors listed above. The values of each contributing factor are shown as a boxplot. A parameter $\delta \in [0,1]$ is introduced, the function of which is to quantify how much high-spatial-frequency spectrum is reconstructed through the planar wave expansion procedure. The variance of the estimation increases with δ as a higher spatial-frequency

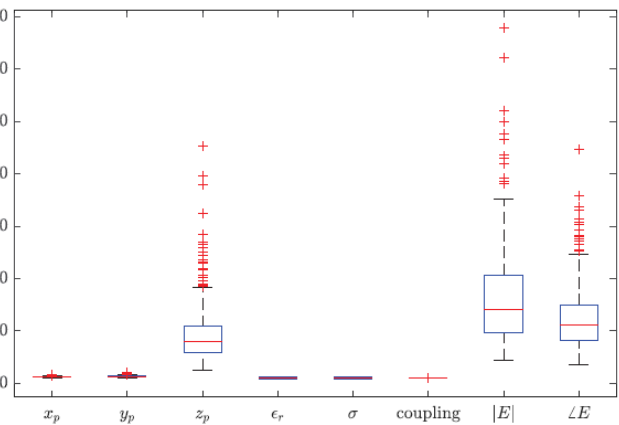
spectrum is reconstructed. From the variance, one identifies the most influential factors. When $\delta = 0$ or 0.01, the uncertainty of relative permittivity and conductivity contributes most to the variation of the estimation. The influence factors are changed as the z coordinate of the probe and the measurement (amplitude and phase) accuracy of the electric field when $\delta = 0.02$ or 0.03. For validation purposes, a further Monte Carlo simulation was independently carried out; the obtained results led to the same conclusion.



(a) $\delta = 0$ and 0.01



(b) $\delta = 0.02$



(c) $\delta = 0.03$

Figure 7. Box plots of estimated values of peak 1 g SAR for the 4th case, fields are reconstructed with the PWE approach by setting various values of δ .

In summary, a method has been developed where uncertainties are propagated through multivariate models, from the initial input parameters such as 2D complex E-field components and phantom electromagnetic properties to the output of the algorithm used for 3D complex E-field reconstruction (through planar wave expansion) and SAR computation. Sources of uncertainties were identified and corresponding sensitivity analysis was carried out.

Objective 3 *Verify the reliability of measurement systems for a wide range of transmitter types and improve the measurement of telecommunication signals and SAR measurement for a wide range of device types. This will include the development of improved data processing used with time-domain probes.*

Three comparisons were performed in order to verify the reliability of vector probe array systems for SAR measurement, involving traditional scanning systems fully compliant with the initial SAR measurement standard (IEEE/IEC 62209-1528), and also standard IEC/IEEE 62704-1 compliant simulated SAR target values:

- Comparison against a traditional scanning measurement system
- Comparison against numerical target values
- Inter-laboratory comparison

ART-FI has set up a comparison implementing several mobile access technologies, modulation and protocols, and involving their vector probe array system ART-MAN and a traditional scanning system, DASY from SPEAG, both available from a SAR certification laboratory, as an independent third party. Comparison on 1 g SAR is presented on Figure 6 and shows equivalence between both systems when the following comparison criteria are applied:

Lower and upper limits for SAR deviation are defined as

$$L = (1 - U_{comb}) \times SAR_{1g, DASY} \text{ and}$$

$U = (1 + U_{comb}) \times SAR_{1g, DASY}$, respectively and where $SAR_{1g, DASY}$ is the peak spatial SAR value measured on DASY system and U_{comb} is the combined uncertainty defined as

$$U_{comb} = \sqrt{U_{ART-MAN}^2 + U_{DASY}^2}$$

with $U_{ART-MAN}$ and U_{DASY} the expanded system uncertainties ($k = 2$) of ART-MAN and DASY, respectively.

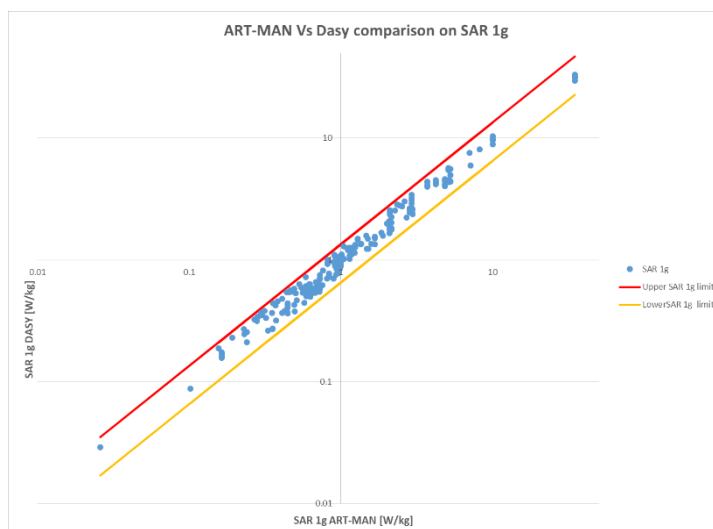


Figure 8: SAR plot and SAR deviation comparison between ART-MAN and DASY

Table 1 presents selected scenarios among the data points of Figure 8. Rightmost columns show 1 g SAR and 10 g SAR measured values for both ART-MAN and DASY systems and corresponding deviations. Here, the SAR of three devices implementing WCDMA, LTE, and WLAN access technologies are measured using different modulation schemes, communication protocols, and positioning.

Table 1: Comparison of a vector array system against a traditional scanning system on several communication configurations

DUT	Techno	Band	BW (MHz)	Modulation	RB Size	RB offset	Mode	Test Position	Gap (mm)	Ch.	Position	Freq. (MHz)	Power Setting	DASY Measured 1g SAR (W/kg)	DASY Measured 10g SAR (W/kg)	ART-MAN Measured 1g SAR (W/kg)	ART-MAN Measured 10g SAR (W/kg)	ARTMAN Vs DASY SAR deviation 1g	ARTMAN Vs DASY SAR deviation 10g
DUT #1	WCDMA	II					RMC12.2Kbps Test mode Loop 1	Rightcheek	0mm	9400		1880		0.28	0.18	0.314	0.189	12%	5%
DUT #1	WCDMA	II					RMC12.2Kbps Test mode Loop 1	Leftcheek	0mm	9400		1880		0.429	0.266	0.377	0.25	-12%	-6%
DUT #1	LTE	7	20M	QPSK	1	0		Rightcheek	0mm	21100		2535		0.472	0.234	0.551	0.291	17%	24%
DUT #1	WCDMA	II					RMC12.2Kbps Test mode Loop 1	Back	0mm	9400	0	1880		5.1	2.27	5.477	2.415	7%	6%
DUT #1	WCDMA	II					RMC12.2Kbps Test mode Loop 1	Back	5mm	9400	0	1880		2.09	0.984	1.891	0.975	11%	8%
DUT #1	WCDMA	II					RMC12.2Kbps Test mode Loop 1	Back	10mm	9400	0	1880		0.94	0.56	0.899	0.5	-15%	-12%
DUT #1	WCDMA	V					RMC12.2Kbps Test mode Loop 1	Back	0mm	4182	0	836.4		4.22	1.87	4.37	1.86	-11%	-6%
DUT #1	WCDMA	V					RMC12.2Kbps Test mode Loop 1	Back	5mm	4182	0	836.4		0.727	0.398	0.577	0.351	-10%	-1%
DUT #1	LTE	7	20M	QPSK	1	0		Back	0mm	21100	0	2535		3.71	1.72	4.014	1.828	0%	9%
DUT #1	LTE	7	20M	QPSK	1	0		Back	5mm	21100	0	2535		0.91	0.466	1.093	0.527	-14%	-6%
DUT #2	LTE	7	20M	QPSK	1	0		Back	0mm	21100	0	2535		5.25	1.96	4.421	1.718	-21%	-13%
DUT #2	LTE	7	20M	QPSK	1	0		Back	10mm	21100	0	2535		4.84	1.97	4.421	1.85	-4%	-11%
DUT #3	WLAN2.4GHz	B					802.11b1Mbps	Back	0mm	1	0	2412	32	1.14	0.433	1.237	0.438	10%	-1%
DUT #3	WLAN2.4GHz	B					802.11b1Mbps	Back	5mm	1	0	2412	32	0.164	0.072	0.164	0.079	-3%	-12%
DUT #3	WLAN5GHz	A					802.11a6Mbps	Front	0mm	36	0	5180	32	34.9	6.98	32.126	7.622	-10%	-16%
DUT #3	WLAN5GHz	A					802.11a6Mbps	Back	5mm	36	0	5180	32	7.06	1.51	7.597	1.549	4%	-1%
DUT #3	WLAN5GHz	A					802.11a6Mbps	Back	5mm	56	0	5280	32	8.21	2.1	8.102	2.172	7%	4%
DUT #3	WLAN5GHz	A					802.11a6Mbps	Back	5mm	116	0	5580	32	7.18	1.77	5.946	1.716	1%	-2%
DUT #3	WLAN5GHz	A					802.11a6Mbps	Back	5mm	157	0	5785	32	2.93	0.785	2.906	0.676	-1%	-5%
DUT #3	WLAN5GHz	A					802.11a6Mbps	Back	10mm	36	0	5180	32	1.89	0.524	1.576	0.471	-21%	-12%

These configurations give an idea on the diversity of scenario's assessed in the framework of this comparison, dealing with the technology, the frequency, the modulation type, the protocol mode, the channel, etc., on both cheek and back exposure figure cases.

Another comparison was carried out where measured SAR values were compared against simulated target values based on numerical modelling (numerical reference) as described in IEC 62209-3 standard and compliant with IEC/IEEE 62704-1 standard.

Table 2 shows such a comparison at all three frequencies (900 MHz, 2450 MHz and 5200 MHz) which were selected in the framework of the project for the development of reference and validation antennas. Deviations on 1 g SAR and 10 g SAR values show equivalence with standard compliant numerical reference SAR values.

Table 2: Comparison against simulated (numerical reference) target values

Frequency	900 MHz	2450 MHz	5200 MHz
Antenna ref.	Dipole 900	Dipole 2450	Dipole 5G
Distance au body (mm)	15	10	10
Position	A1	A0	A0
Orientation	0°	0°	0°
Forward power (dBm)	17	24	20
Forward power (W)	0.05	0.25	0.1
Duty cycle	100%	100%	100%
1 g SAR Meas.	0.556	12.32	7.391
10 g SAR Meas.	0.364	5.639	2.081
1 g SAR Target	0.547	12.911	7.65
10 g SAR Target	0.35	5.978	2.16
1 g Dev. SAR (%)	1.58	-4.58	-3.38
10 g Dev. SAR (%)	3.92	-5.68	-3.68

Finally, an inter-laboratory comparison was arranged, involving four partners using three different technologies: two traditional scalar probe robotic scanning systems used by NPL and TUBITAK, an automated vector probe scanning system used by LNE and a vector array system used by ART-FI.

All four partners including LNE and TUBITAK have set up and conditioned their systems government preventive measures for this comparison, but because of the COVID-19 pandemic, only two partners, NPL and ART-FI were able to carry out their measurements before government preventive measures were taken across Europe, by the end of the project.

Three reference dipoles as described in IEC 62209-3 standard and working at the selected frequencies (900 MHz, 2450 MHz and 5200 MHz) were used as comparison devices.

Both partners handled to carry out their measurements on a flat phantom, with configurations that are as close as possible to each other, in terms of delivered power, tissue equivalent liquid electromagnetic characteristics, dipole positioning against the phantom (under and above the phantom for NPL and ART-FI configurations, respectively). Measurements are presented in Figure 8, for 900 MHz, 2450 MHz and 5200 MHz reference dipoles, respectively. One can note that the grid size is smaller for NPL compared to ART-FI presentation of the results.

These results can be used, once corrected for differences in delivered power, tissue equivalent liquid electromagnetic characteristics and dipole positioning, to validate ART-FI's vector array system against a system which establishes traceability to SI such as the one from NPL.

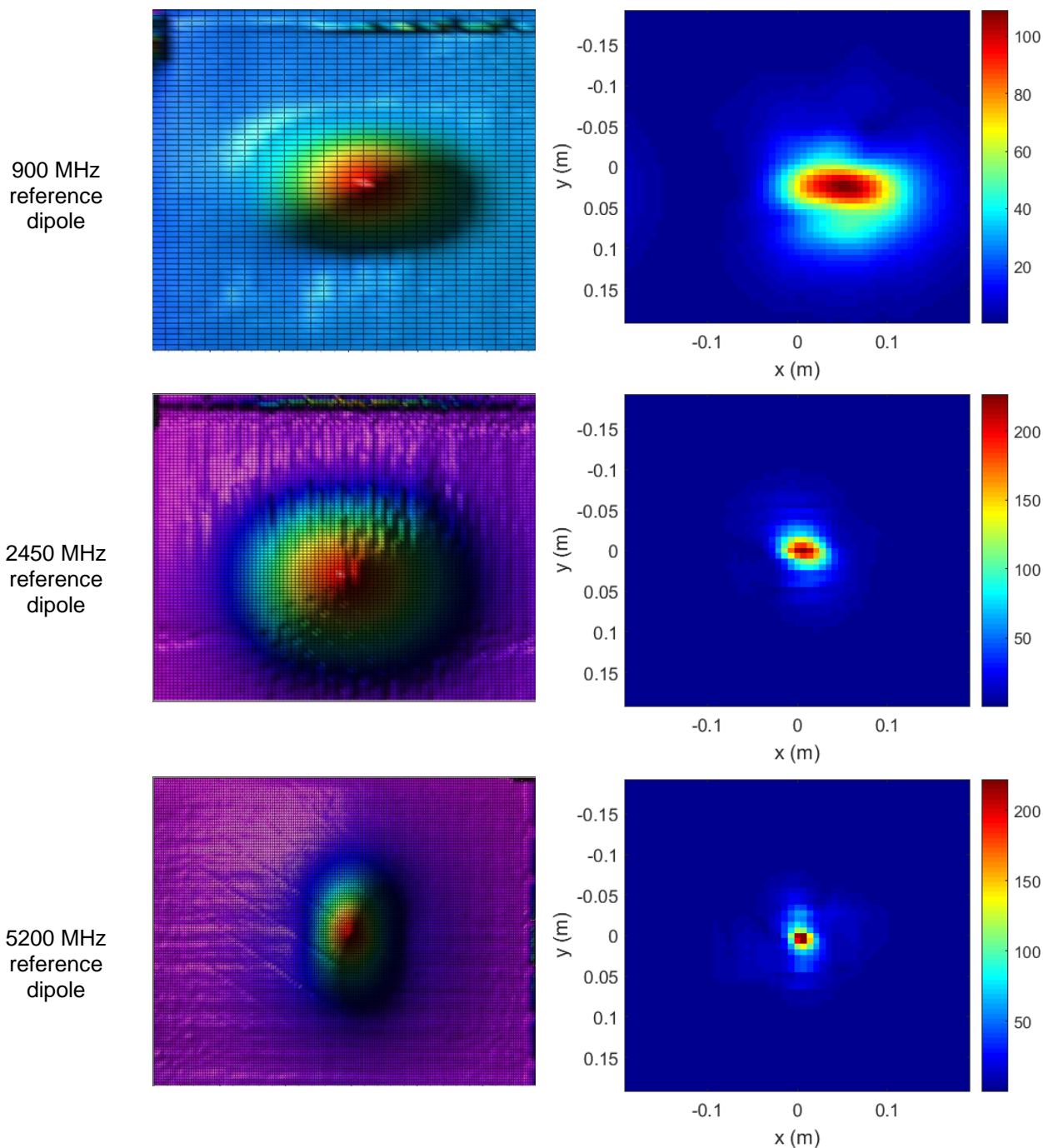


Figure 8: Total applied electric field at 900 MHz, 2540 MHz and 5200 MHz, as scanned by NPL system (left) and measured and reconstructed by ART-FI system (right)

In summary, the reliability of vector probe arrays has been verified through several comparison processes and data processing applicable to time-domain probes, with independent methodologies and validation assessment criteria and involving a wide range of transmitter types.

Objective 4 Develop test protocols for MIMO devices using vector probe arrays in order to determine the maximum SAR value (worst case) by combining MIMO signal figures.

The aim was to provide a test protocol, specify the requirements for the sample rate and averaging time for accurately determining the spatial peak 1 g or 10 g SAR from MIMO devices using vector probe arrays, and provide methods for assessing the peak spatial averaged SAR from MIMO systems with beam forming capability.

Three methods and procedures were developed by ART-FI for the assessment of the MIMO-SAR using a vector SAR measurement system. An experimental MIMO demonstrator shown in Figure 9 was set up by exploiting the characteristics of such vector probe measurement system. It implements two dipoles with different orientations, connected to two different signal generators with power monitoring and local oscillator synchronisation enabling control of the phase shift between the two signals.

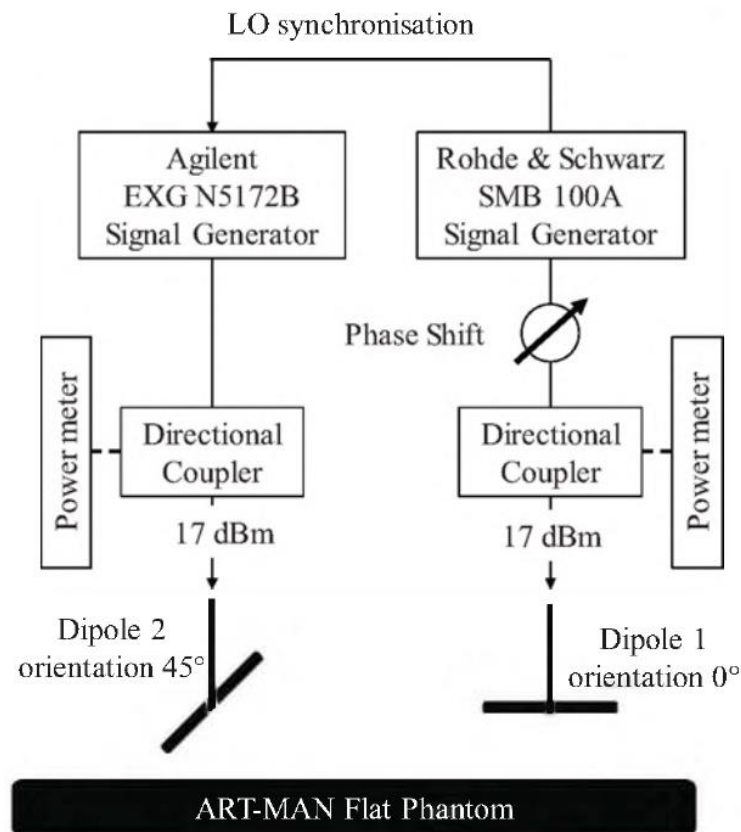


Figure 9. Block diagram of the experimental MIMO set-up

First, a fast and efficient procedure was introduced by ART-FI for the assessment of the MIMO-SAR on a vector SAR measurement system, but that takes as a phase reference-wave the electric field of the antenna under test for measuring the electric field phasor vector. It uses the measurements of the vector electric-field data from the individual antenna-array elements, and at least an additional measurement of simultaneous excitation of the antenna-array. The true SAR level of the MIMO system is then assessed through post-processing by linearly combining the individual field data weighted by all the array configuration coefficients.

The vector SAR system used was model ART-MAN of their brand, which is planar near-field measurement system which enables measurement of the time-independent complex E-field phasor vector in a broadband human tissue simulant material. The time-domain vector E-field probe array consists in a grid of dual-polarized sensors made for capturing two orthogonal E-field components tangential to the measurement surface. Near-field vector techniques directly exploit the harmonic property of the electromagnetic field, allowing the three E-field components (x, y, z) in all three dimensions to be deduced from the knowledge of amplitude and phase of E-field components (E_x and E_y) tangential to a surface.

Assessing vector fields requires determining the phase relative to a preselected probe element among the probe array, used as a reference, through synchronous and coherent acquisition of the probe voltage time-series on the measurement and the reference probes through a two-way radio frequency chain.

The main steps of the proposed procedure for the assessment of the actual peak volume-averaged SAR for the two-antenna MIMO system are defined as follows.

- Step#1: The vector E-field for sequential excitation of each one of the two antenna ports are measured one after the other, while the other port is terminated with matched load, for an equal and monitored incident power. Hence one obtains at the probe plane, defined by $z = z_0$, $E_1(x, y, z_0)$ for the excitation at Dipole-1's port and $E_2(x, y, z_0)$ for the excitation at Dipole-2's port.
- Step#2: The vector E-field for simultaneous excitation at all of the two antenna ports is measured for equal incident power and an enforced phase shift φ_0 on the two signal generators. A combined total field $E_{cmb}(x, y, z_0)$ is obtained at the probe plane.
- Step#3: The field measurement results of Step#1 and Step#2 are employed to retrieve the phase-shift β that minimizes the root mean square error on the amplitude of the measured $|E_{cmb}|$ and superimposed $|E_1 + E_{2,p} \cdot e^{j(\varphi_0 + \beta)}|$ of the two E-field measurements in Step#1.
- Step#4: The total E-field from the antenna array at all its interference states, defined by the complex weights $(\alpha_{i=1:M}, \gamma_{i=1:M})$ of the antenna array ports, are computed as $E_{cmb.i}(x, y, z) = \sum_{i=1}^M \alpha_i \cdot E_1(x, y, z) + \gamma_i \cdot E_2(x, y, z) e^{j\beta}$
- Step#5: For each array interference state $i = 1; M$, the volume SAR is computed and the 1 g cube and 10 g cube averaging algorithm, as per IEEE 1528 standard, is employed to evaluate the actual peak volume averaged SAR of the MIMO system.

Example of E-field measurement data for simultaneous feed of the dipoles with $3\pi/4$ phase shift and for the retrieved E-field are shown in Figure 10.

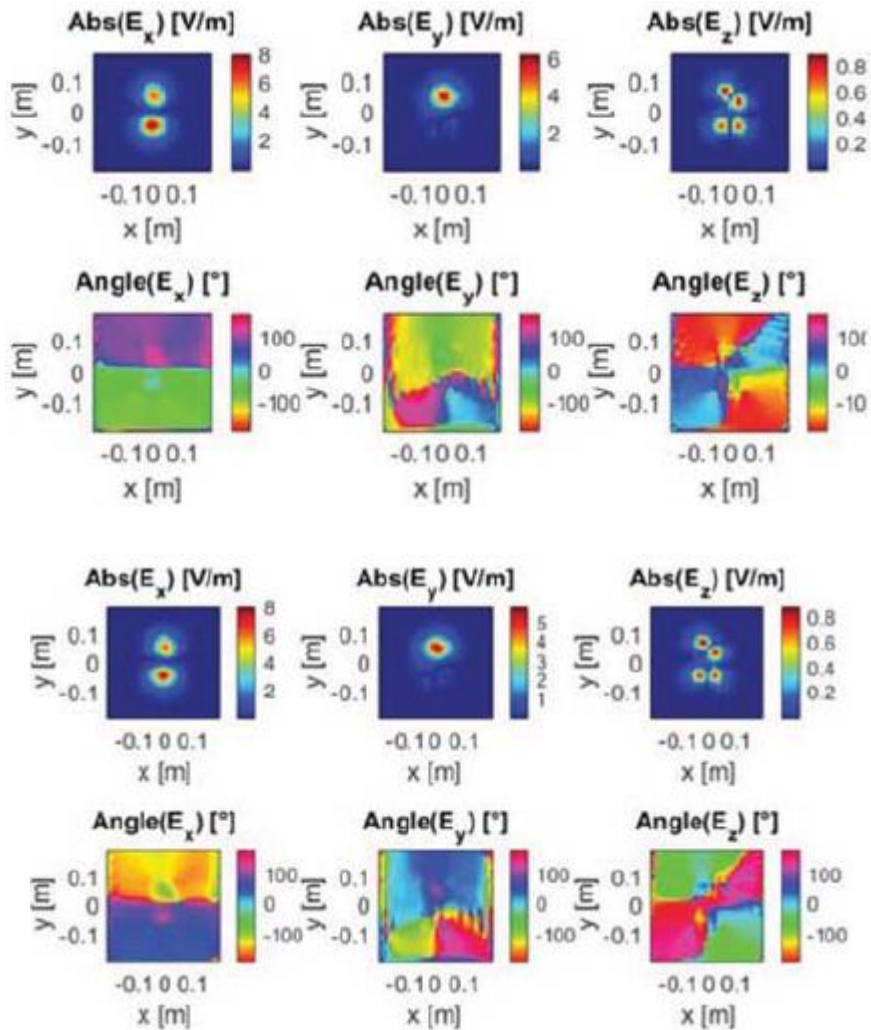


Figure 10. Measured (up) and retrieved (down) E-field for simultaneous feed of the dipoles with $3\pi/4$ phase shift.

Second, a similar procedure has then been proposed, including the phase calibration method, but for the case of MIMO systems that feature exclusive simultaneous excitations of the antenna array. Indeed, in most practical cases, the excitation of a MIMO system is exclusively simultaneous and the power is uniformly distributed between all the antennas. In this case, the SAR value for any arbitrary configuration of the MIMO system (defined by the excitation weights w_i) can be obtained by performing a proposed procedure detailed below.

- Step#1: Perform N measurements of the electric field phasor $E_m^{meas} = \sum_{i=1}^N w_{mi} \cdot E_i$ (with $m = 1, \dots, N$) for MIMO configurations with exclusively simultaneous excitations (i.e.: $w_{mi} \neq 0, \forall m, i \in \{1, \dots, N\}$). w_{mi} is the excitations weight of the i^{th} MIMO antenna used for the m^{th} measurement.
- Step#2: Perform at least one “test” measurement $E_m^{\text{test}} = \sum_{i=1}^N w_{ti} \cdot E_i$ with excitation weights different from the ones used in Step#1 in order to align the phase references of all of the N measurements.
- Step#3: Use the fields measured in Step#1 and Step#2 in order to calibrate and to align the phase reference of the different measurements. This is achieved by introducing a set of phase shifts β_m (with $m = 1, \dots, N$) on the measured fields E_m^{meas} and by minimizing the deviation between the initial measured field and the complementary “test” measurement.

- Step#4: Retrieve the electric field E_i corresponding to each individual antenna of the MIMO system from inverse equation of step#1.
- Step#5: Compute the electric field E corresponding to any relevant MIMO excitation scheme.
- Step#6: For each MIMO configuration, compute the peak volume-averaged SAR of the system for the compliance assessment purpose.

An experimental validation set-up similar to the one of Figure 9 is used: the two dipoles were excited using exclusively simultaneous excitations in order to perform two initial measurements of the electric field (Step#1) and a third additional test measurement for phase alignment (Step#2). A comparison between the retrieved and measured SAR 1 g and 10 g values are represented in Figure 11 and show a very good agreement (less than 3.5% error). The conservative SAR value that one obtains if only the amplitude of the E-fields is measured is also shown. It can be seen that the true SAR value is up to 15% smaller than the conservative SAR value.

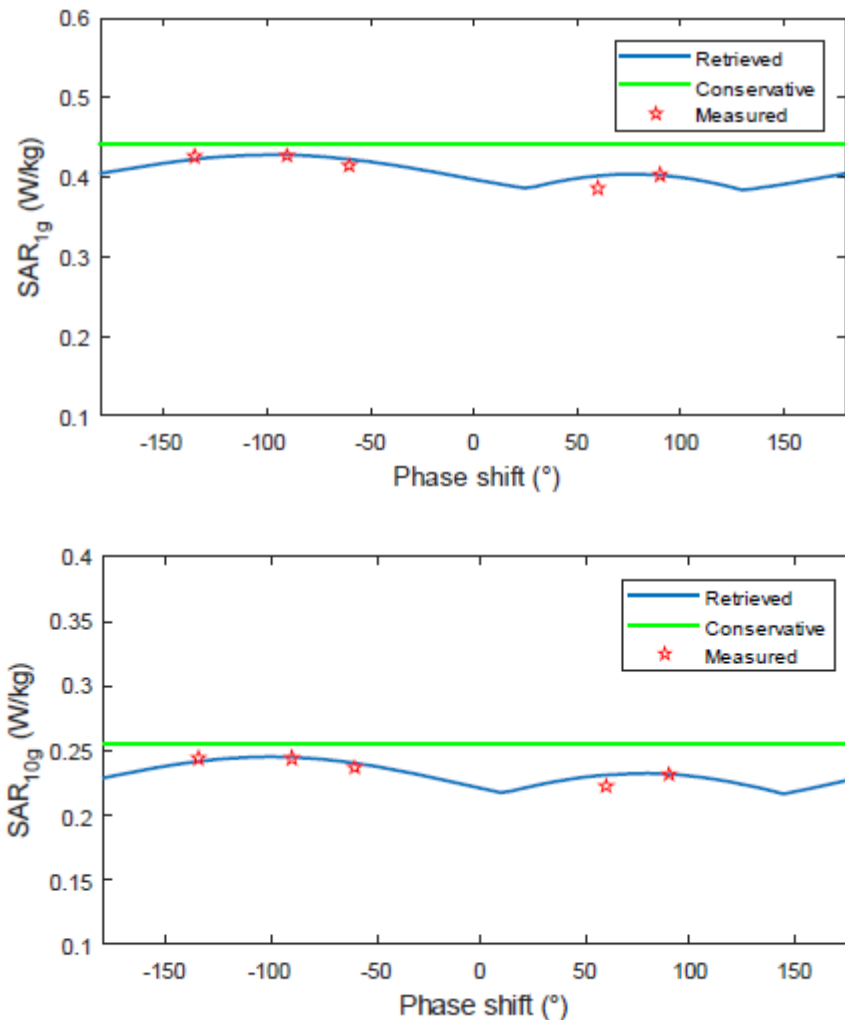


Figure 11. Measured (red), retrieved (blue) a amplitude only measurement conservative value (green) for 1 g (up) and 10 g (down).

Finally, a method was also proposed to determine SAR for MIMO signals with rapid variation. In this case, it can be noted that the determination of the time average of the SAR of a MIMO system is the determination of the individual SARs resulting from the individually excited antennas, as well as the averages of the

squares of the system excitation signals. Hence, a measurement method consisting of two main steps allowing to determine the average SAR of an N-antenna MIMO system can be defined as follows.

Step 1 - Configuration with small time variation:

- a. Force the DUT to operate in a configuration with slow variation.
- b. Follow the method presented in the first procedure above in order to determine, from N+1 measurements, the individual SARs $SAR_i(x, y, z)$ resulting from the separate excitation of the MIMO antennas, in points (x, y, z) of the measurement domain.

Step 2 - Configuration with rapid variation:

- a. Put the DUT in its nominal configuration of strong time variation of the relative phases and for which the SAR measurement is to be performed.
- b. Measure the instantaneous local SAR at K points ($K \geq N$) of the grid of the sensor array, and over a period T long enough to reach the convergence of the SAR time average $\langle SAR \rangle$.
- c. From these SAR averages and individual SARs determined in step 1, determine the mean value of the squares of the excitation signals.
- d. Determine the value of the temporal average SAR at any point in space (x, y, z) .

An implementation example of this procedure applied to a two antenna MIMO system shows that only three vector SAR measurements with an average duration of 15 s each and two time-averaged SAR measurements (80 μ s per measurement) at two points in space are needed. Results obtained are shown in Figure 12.

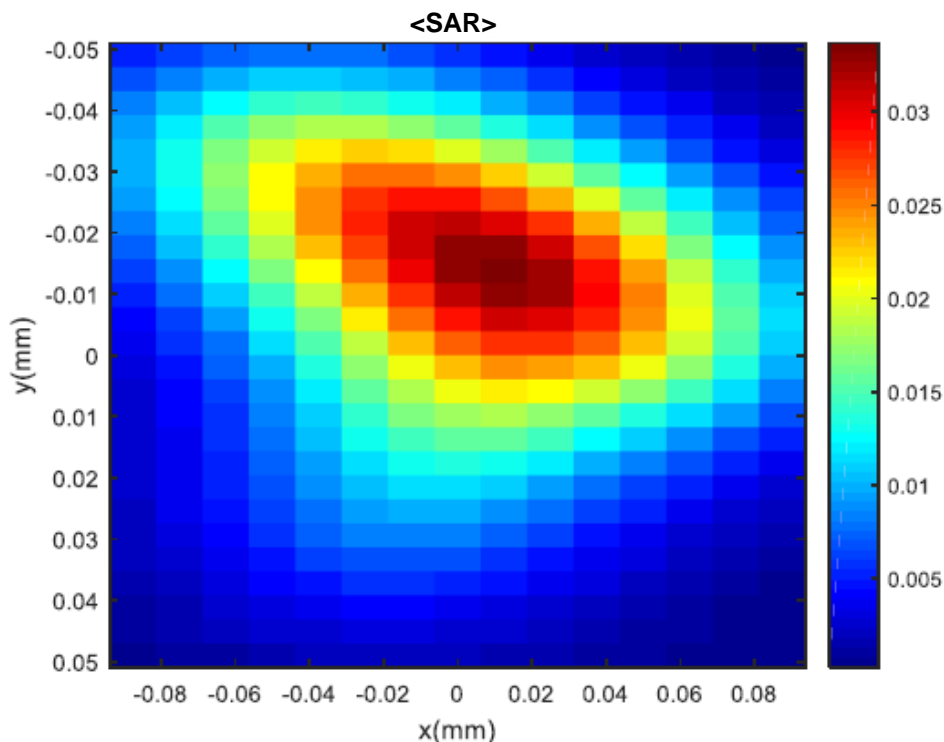


Figure 12. Example of a 2 MIMO antenna system retrieved local SAR distribution, averaged over time.

In summary, several protocols were developed for testing MIMO devices using vector probe arrays, which allows determining the maximum SAR value when MIMO signal figures are combined. This concerns several configurations with regard to phase reference definition, and for the cases of exclusive simultaneous excitations and of rapid variations, consistent with existing real cases.

5. Impact

The project formed a stakeholder committee of nine members from mobile phone and other communications technologies manufacturers, and research organisations. Most of these members participated in the standardisation process together with consortium partners and therefore dissemination on the progress of the project was made easier. Nine presentations have been given in international and national conferences. Three open access proceedings papers and three peer-reviewed papers were published in international journals. The consortium was also able to organise i) an interactive online training course for Industry members, ii) one to one training among consortium partners to share knowledge on E-field calibration and isotropy/directivity and linearity characterisation, and iii) a workshop on SAR Best Practices Seminar.

Impact on industrial and other user communities

This project will enable manufacturers of vector-based SAR measurement equipment to have better quality control of their products and will provide greater confidence in their measurement accuracy. The consortium included two of these manufacturers (ART-FI and KAPTEOS) and other manufacturers of these systems were encouraged to join the stakeholder committee and collaboration was set up with an alternative manufacturer. A Skype training course dedicated to industry members was provided in conjunction with a standardisation TC meeting. Moreover, a secondment was arranged between NPL and KAPTEOS where KAPTEOS personnel could use NPL facilities and gain expertise in E-field calibration, isotropy/directivity and linearity characterisation. The result was the validation of the KAPTEOS vector probes in terms of performances at NMI level. The wider impact to industry will be achieved by the incorporation of the results into future revisions of IEC 62209-3 standard, which will enable to improve reliability in the use of these systems by test houses for testing full compliance of mobile telecoms devices against exposure limits. This will result in considerable cost savings for device manufacturers and will reduce the time to bring new products to market. This will also reduce the significant costs associated with the annual calibration of the validation antenna set by around 75% compared with existing methods in the standard, so offers significant advantage to the users of these systems. It will also increase public confidence on the safety of the devices.

Impact on the metrology and scientific communities

The outputs of the project will enhance the partners' knowledge of metrology for EMF safety and of the statistical analysis of vector-based SAR measurement systems, leading to further metrological advances in these areas. Results were shared with the wider scientific community through presentations at international conferences, and an opportunity was taken at one of these conferences to hold a booth and present a poster in a dedicated session where several stakeholders from Europe and worldwide have been approached and informed on the status of the project regarding the IEC 62209-3 standard. The project's results have also been presented to CCEM-GTRF and EURAMET TC-EM RF&MW. These two subcommittees report then to CIPM-CCEM and EURAMET-TC-EM committees. Full open access was provided to datasets, software tools and documentary reports. The project website and other databases, e.g. the partners' websites, will be used as platforms to facilitate new scientific studies in this and related areas.

Impact on relevant standards

This project will be crucial for future revisions of the IEC 62209-3 standard by providing the required calibration and uncertainty analysis methods and text. The partners liaised with IEC - TC 106, in particular with the IEC - TC 106/PT 62209-3. Several partners are part of this working group, which have been developing the IEC 62209-3 standard to disseminate the outputs of this project and seek feedback, so that they can be incorporated into future revisions of this standard. Results were shared with IEC TC106 'Methods for the assessment of electric, magnetic and electromagnetic fields associated with human exposure', in particular i) MT1 (responsible for the maintenance of IEC 62209-1), ii) MT3 (responsible for the maintenance of IEC 62232), iii) PT 62704-4 'Determining the Peak Spatial-Average Specific Absorption Rate (SAR) in the Human Body from Wireless Communications Devices, 30 MHz - 6 GHz - Part 1:General Requirements for using the Finite-Difference Time-Domain (FDTD) Method for SAR Calculations' and iv) JWG13 (responsible for IEC/IEEE 62209-1528 ED1 Measurement procedure for the assessment of specific

absorption rate of human exposure to radio frequency fields from hand-held and body-worn wireless communication devices - Part 1528: Human models, instrumentation and procedures (Frequency range of 4 MHz to 10 GHz). Additionally, the project has been presented to CENELEC TC 106X 'Electromagnetic fields in the human environment'. Final results such as written reports and guides that are suitable for adoption into the standards will be implemented through dissemination to the wider IEC - TC 106 committee to facilitate the development of standards on EMF safety of other devices and the development of standards in support of 5G, which is a stated priority of the IEC - TC 106.

Longer-term economic, social and environmental impacts

This project will ensure that 5G device compliance with safety limits for EMF can be demonstrated, which is an essential step in the implementation of this new technology. This will help i) to move towards a harmonised set of standards for assessing SAR from wireless devices, ii) to allow a dramatic cost reduction of bringing new LTE smartphone models to market thanks to reduction in the measurement time from a few weeks with a single probe to a few hours with a vector probe array and iii) to allow reduction of global power consumption thanks to efficient strategies for assessing SAR from MIMO and beamforming technologies. This work will also facilitate the introduction of MIMO, LTE 4G, 5G and IoT devices by ensuring that their EMF safety can be assessed, in line with the increasing demands of users for network data capacity.

6. List of publications

D. Allal, "EMPIR European project for validation of vector array SAR measurement systems", 19th International Congress of Metrology, Paris, 2019, <https://doi.org/10.1051/metrology/201902003>

L. Aberbour, "Efficient Experimental Assessment of the Specific Absorption Rate (SAR) induced by MIMO Wireless Communication Devices; Application of Vector Near-Field Measurement System", 2018 IEEE Conference on Antenna Measurements & Applications (CAMA), <https://hal.archives-ouvertes.fr/hal-02376333>

Liu, Z.; Allal, D.; Cox, M.; Wiart, J. Discrepancies of Measured SAR between Traditional and Fast Measuring Systems. *Int. J. Environ. Res. Public Health* **2020**, *17*, 2111, <https://doi.org/10.3390/ijerph17062111>

Gregory, A.P.; Quéléver, K.; Allal, D.; Jawad, O. Validation of a Broadband Tissue-Equivalent Liquid for SAR Measurement and Monitoring of Its Dielectric Properties for Use in a Sealed Phantom. *Sensors* **2020**, *20*, 2956, <https://doi.org/10.3390/s20102956>

Liu, Z.; Allal, D.; Cox, M.; Wiart, J. Reply to "Comment on Liu et al. 'Discrepancies of Measured SAR between Traditional and Fast Measuring Systems' *Int. J. Environ. Res. Public Health*, 2020, 17, 2111", <https://doi.org/10.3390/ijerph17155355>

M. Teniou, O. Jawad, S. Pannetrat and L. Aberbour, "A Fast and Rigorous Assessment of the Specific Absorption Rate (SAR) for MIMO Cellular Equipment Based on Vector Near-Field Measurements," 2020 14th European Conference on Antennas and Propagation (EuCAP), Copenhagen, Denmark, 2020, pp. 1-5, <https://hal.archives-ouvertes.fr/hal-02954816>

7. Contact details

Djamel Allal (djamel.allal@lne.fr)